AIAA 99-0185

Aerodynamic Shape Inverse Design Using a Fourier Series Method

G. S. Dulikravich and D. P. Baker
The Pennsylvania State University
University Park, PA

37th AIAA Aerospace Sciences Meeting and Exhibit
January 11-14, 1999 / Reno, NV

AIAA 99-0185

AERODYNAMIC SHAPE INVERSE DESIGN USING A FOURIER SERIES METHOD

George S. Dulikravich* and Daniel P. Baker+
Department of Aerospace Engineering, 233 Hammond Building
The Pennsylvania State University, University Park, PA 16802
ft7@psu.edu

Abstract

An approach to the aerodynamic inverse shape design problem is considered where the shape update at each iteration is found using an analytical Fourier series solution to a set of two linear differential equations with interrelated boundary conditions. The design technique requires knowledge only of the surface pressure distribution on the body to perform a shape update. Thus, it can be implemented without modifying an existing aerodynamic flow-field analysis code. Formulations are given for both the two-dimensional airfoils and three-dimensional wings. The Fourier design technique was successfully tested in conjunction with a panel code, an Euler code, and a turbulent Navier-Stokes flow-field analysis code, at subsonic and transonic speeds. The Fourier series method was found to converge within 6-25 flow-field analysis while simultaneously determining spanwise variation of wing thickness, camber, twist, and dihedral.

I. Introduction

Aerodynamic shape design can broadly be classified into two categories: shape optimization and inverse shape design[1-4]. The shape optimization approach attempts to find the best global aerodynamic properties from the design. On the other hand, the inverse shape design approach requires that specific local properties of the final configuration be specified as goals of the design.

The inverse aerodynamic shape design is defined as follows: given a desirable surface pressure distribution on an aerodynamic body, find the shape of the body that will achieve this pressure distribution subject to a given global flow condition. There exist a multitude of inverse design techniques that are useful in solving different types of engineering problems[1-8].

Two major classes of inverse design tools for aerodynamic shape design can be defined: methods with coupled analysis and shape modification, and methods with uncoupled analysis and shape modification.

The coupled methods require special consideration in the writing of the flow-field analysis code. For example, an indirect transpiration technique[3, 4] might exchange no-slip wall boundary conditions on the body with specified pressure boundary conditions in order to obtain a shape update. Other examples of this class of techniques are: stream-function-as-coordinate approaches, characteristic boundary condition approaches, and adjoint operator/control theory approaches[3,4].

On the other hand, uncoupled inverse methods require no modification to a flow-field analysis tool. Thus, any reliable flow-field analysis code (a panel code, a Navier-Stokes code, or even a wind tunnel data) can be used in the design process without a need for alterations of such an analysis tool. For example, elastic membrane techniques[9-14] require knowledge of only the surface pressure distribution on the current aerodynamic shape as an output from the flow-field analysis code in order to predict a shape update. The DISC technique is another example of such a technique[15]. Because they are uncoupled from the flow-field analysis, these design techniques have the added benefits of simplicity, relative ease of programming, and versatility.

II. MGM Elastic Membrane Techniques

Garabedian and McFadden[9,10] first proposed the elastic membrane approach to aerodynamic inverse shape design. The technique treats the surface of an aerodynamic body as a membrane that deforms under aerodynamic loads until it achieves a desired surface pressure distribution. The original model[9,10] for the evolution of an airfoil shape was given by

$$\beta_0 \Delta n + \beta_1 \frac{d\Delta n}{dx} + \beta_2 \frac{d^2 \Delta n}{dx^2} = C_p^{target} - C_p^{actual} \qquad (1)$$

Here, Δn's are defined as shape corrections along outward normal vectors (Fig. 1), and $\beta_{0\text{-}2}$ are user supplied

---

* Associate Professor. Associate Fellow AIAA.
+ NASA Graduate Student Fellow. Student member AIAA.

constants that control the rate of convergence of the shape evolution process, while C_p^{target} and C_p^{actual} are the specified (target) and the actual (computed) local surface pressure coefficients, respectively. This technique was modified by Malone et al.[11], giving

$$\beta_0 \Delta y + \beta_1 \frac{d\Delta y}{dx} + \beta_2 \frac{d^2 \Delta y}{dx^2} = C_p^{target} - C_p^{actual} \qquad (2)$$

With this formulation (dubbed MGM for modified-Garabedian-McFadden or Malone-Garabedian-McFadden) all shape modifications are in the y-direction, thus preventing the chord length from changing. The MGM shape evolution equation (2) is traditionally solved for Δy shape corrections using a finite difference approach by discretizing along the airfoil contour. The following formulation assumes that the index numbering proceeds clockwise, starting from the trailing edge of the airfoil. Using central difference formulae for the derivatives in equation (2) results in a tridiagonal set of linear, algebraic equations for the unknown y-coordinate updates.

$$A_i \Delta y_{i-1} + B_i \Delta y_i + C_i \Delta y_{i+1} = C_{p_i}{}^{target} - C_{p_i}{}^{actual} \qquad (3)$$

Two major problems with the classical MGM approach are its slow convergence at the leading and trailing edges of the airfoil, and its significantly slower convergence in conjunction with the flow-field analysis codes of increasing non-linearity[14].

III. Fourier Series Elastic Membrane Approach to Aerodynamic Design

In an attempt to alleviate these problems, a new formulation of the elastic membrane concept has been devised[16-18]. It allows a Fourier series analytical solution to the shape evolution equation.

A. Fourier Series Aerodynamic Inverse Design in Two Dimensions

Equation (2) can be expressed by two different equations on the top and bottom airfoil contours, as the signs of two β coefficients must change for symmetry. On the upper airfoil contour,

$$-\beta_0 \Delta y + \beta_s \frac{d\Delta y}{ds} + \beta_{ss} \frac{d^2 \Delta y}{ds^2} = \Delta C_p \qquad (4)$$

where s is the airfoil contour-following coordinate (Fig. 1). Then, on the lower airfoil contour,

$$\beta_0 \Delta y + \beta_s \frac{d\Delta y}{ds} - \beta_{ss} \frac{d^2 \Delta y}{ds^2} = \Delta C_p \qquad (5)$$

These two ordinary differential equations with constant coefficients are reminiscent of a well-known forced mass-damper-spring system.

It is important to recognize the analogy between the monotonically increasing time coordinate in the forced mass-damper-spring system and the monotonically increasing contour following coordinate, s, in the Eqs. (4) and (5).

Also, it is important to recognize the analogy between the forcing function in the mass-damper-spring system which varies arbitrarily with time and the surface pressure coefficient difference, ΔC_p, which varies arbitrarily with the contour following coordinate, s, in Eqs. (4) and (5).

Finally, there is an analogy between the global periodicity of the mass-damper-spring forcing function and the global periodicity of the surface pressure coefficient difference, ΔC_p, which repeats its value at the starting and the ending contour-following s-coordinate location (Fig.1).

Then, ΔC_p in Eqs. (4) and (5) can be represented by utilizing the Fourier series expansion of the form

$$\Delta C_p(s) = a_0 + \sum_{n=1}^{n_{max}} [a_n \cos(N_n s) + b_n \sin(N_n s)] \qquad (6)$$

where

$$N_n = \frac{2n\pi}{L} \qquad (7)$$

and L is the total length of the airfoil contour.

The particular solution of either Eq. (4) or Eq. (5) can be represented in the general Fourier series form

$$\Delta y_p = A_0 + \sum_{n=1}^{n_{max}} [A_n \cos(N_n s) + B_n \sin(N_n s)] \qquad (8)$$

Then,

$$\frac{d\Delta y_p}{ds} = \sum_{n=1}^{n_{max}} [-A_n N_n \sin(N_n s) + B_n N_n \cos(N_n s)] \qquad (9)$$

$$\frac{d^2 \Delta y_p}{ds^2} = \sum_{n=1}^{n_{max}} [-A_n N_n^2 \cos(N_n s) - B_n N_n^2 \sin(N_n s)] \qquad (10)$$

Substitution of Eqs. (6)-(10) into the airfoil top contour evolution equation (4) yields

$$A_n^{top} = \frac{a_n(\beta_0 + N_n{}^2\beta_{ss}) - b_n(\beta_s N_n)}{(\beta_0 + N_n^2\beta_{ss})^2 + (\beta_s N_n)^2}, n = 0,1,2,\cdots \tag{11}$$

$$B_n^{top} = \frac{b_n(\beta_0 + N_n^2\beta_{ss}) + a_n(\beta_s N_n)}{(\beta_0 + N_n^2\beta_{ss})^2 + (\beta_s N_n)^2}, n = 1,2,3,\cdots \tag{12}$$

Similarly, substitution of Eqs. (6)-(10) into the lower airfoil contour evolution equation (5), results in

$$A_n^{bottom} = \frac{a_n(-\beta_0 - N_n{}^2\beta_{ss}) - b_n(\beta_s N_n)}{(\beta_0 + N_n{}^2\beta_{ss})^2 + (\beta_s N_n)^2}, n = 0,1,2,\cdots \tag{13}$$

$$B_n^{bottom} = \frac{b_n(-\beta_0 - N_n{}^2\beta_{ss}) + a_n(\beta_s N_n)}{(\beta_0 + N_n{}^2\beta_{ss})^2 + (\beta_s N_n)^2}, n = 1,2,3,\cdots \tag{14}$$

Since the Fourier coefficients of the particular solutions on the upper and lower airfoil contours are different, it can be expected that gaps will form at the leading and trailing edges of the airfoil. These gaps can be closed with appropriate homogeneous solutions to Eqs. (4) and (5).

The upper contour homogenous solution is

$$\Delta y_h^{top} = F^{top} e^{\lambda_1 s} + G^{top} e^{\lambda_2 s} \tag{15}$$

where

$$\lambda_{1,2} = \frac{\beta_s \pm \sqrt{\beta_s{}^2 + 4\beta_0\beta_{ss}}}{2\beta_{ss}} \tag{16}$$

and F and G are as yet undetermined coefficients.

Likewise, on the lower airfoil contour, the homogeneous solution is

$$\Delta y_h^{bottom} = F^{bottom} e^{-\lambda_1 s} + G^{bottom} e^{-\lambda_2 s} \tag{17}$$

Thus, the overall displacement (correction) of the airfoil contour is given by the following equations:

$$\Delta y^{top} = F^{top} e^{\lambda_1 s} + G^{top} e^{\lambda_2 s} + \sum_{n=0}^{n_{max}} \left[A_n^{top} \cos(N_n s) + B_n^{top} \sin(N_n s)\right] \tag{18}$$

$$\Delta y^{bottom} = F^{bottom} e^{-\lambda_1 s} + G^{bottom} e^{-\lambda_2 s} + \sum_{n=0}^{n_{max}} \left[A_n^{bottom} \cos(N_n s) + B_n^{bottom} \sin(N_n s)\right] \tag{19}$$

The four unknown constants F and G can now be determined for the upper and lower airfoil contours such that the following four boundary conditions are met: trailing edge closure, zero trailing edge displacement, leading edge closure, and smoothness of Δy at the leading edge.

For zero trailing edge displacement,

$$\Delta y^{bottom}(0) = 0 \tag{20}$$

For trailing edge closure,

$$\Delta y^{bottom}(0) = \Delta y^{top}(L) \tag{21}$$

From Eqs. (20) and (18) it follows that

$$F^{bottom} + G^{bottom} = -\sum_{n=0}^{n_{max}} A_n^{bottom} \tag{22}$$

From Eqs. (21) and (19) it follows that

$$F^{top} e^{L\lambda_1} + G^{top} e^{L\lambda_2} = -\sum_{n=0}^{\infty} A_n^{top} \tag{23}$$

For leading edge closure,

$$\Delta y^{bottom}(s_{LE}) = \Delta y^{top}(s_{LE}) \tag{24}$$

From Eqs. (24), (18) and (19) it follows that

$$F^{bottom} e^{-s_{LE}\lambda_1} + G^{bottom} e^{-s_{LE}\lambda_2} - F^{top} e^{s_{LE}\lambda_1} - G^{top} e^{s_{LE}\lambda_2} = \sum_{n=0}^{n_{max}} [\Delta A_n \cos(N_n s_{LE}) + \Delta B_n \sin(N_n s_{LE})] \tag{25}$$

where

$$\Delta A_n = A_n^{top} - A_n^{bottom}\ ;\ \Delta B_n = B_n^{top} - B_n^{bottom} \tag{26}$$

For smooth leading edge deformation,

$$\frac{d}{ds}\Delta y^{bottom}(s_{LE}) = \frac{d}{ds}\Delta y^{top}(s_{LE}) \tag{27}$$

From Eqs. (27), (18) and (19) it follows that

$$-F^{bottom}\lambda_1 e^{-s_{LE}\lambda_1} - \lambda_2 G^{bottom} e^{s_{LE}\lambda_2}$$
$$-F^{top}\lambda_1 e^{s_{LE}\lambda_1} - G^{top}\lambda_2 e^{s_{LE}\lambda_2}$$
$$= \sum_{n=0}^{n_{max}} [-N_n \Delta A_n \sin(N_n s_{LE}) + N_n \Delta B_n \cos(N_n s_{LE})] \tag{28}$$

Simultaneous solution of Eqs. (22), (23), (25), and (28) for the unknown coefficients F and G results in

$$\begin{Bmatrix} F^{bottom} \\ G^{bottom} \\ F^{top} \\ G^{top} \end{Bmatrix} =$$

$$\begin{bmatrix} 1 & 1 & 0 & 0 \\ 0 & 0 & e^{L\lambda_1} & e^{L\lambda_2} \\ e^{-s_{LE}\lambda_1} & e^{-s_{LE}\lambda_2} & -e^{s_{LE}\lambda_1} & -e^{s_{LE}\lambda_2} \\ -\lambda_1 e^{-s_{LE}\lambda_1} & -\lambda_2 e^{-s_{LE}\lambda_2} & -\lambda_1 e^{s_{LE}\lambda_1} & -\lambda_2 e^{s_{LE}\lambda_2} \end{bmatrix}^{-1} \cdot$$

$$\begin{Bmatrix} -\sum_{n=0}^{n_{max}} A_n^{bottom} \\ -\sum_{n=0}^{n_{max}} A_n^{top} \\ \sum_{n=0}^{n_{max}} [\Delta A_n \cos(N_n s_{LE}) + \Delta B_n \sin(N_n s_{LE})] \\ \sum_{n=0}^{n_{max}} [-N_n \Delta A_n \sin(N_n s_{LE}) + N_n \Delta B_n \cos(N_n s_{LE})] \end{Bmatrix} \tag{29}$$

B. Fourier Series Aerodynamic Inverse Design in Three Dimensions

The two-dimensional Fourier series shape evolution equation can be expanded to three dimensions as follows. First, define a second surface-following coordinate, t, beginning at the wing root and extending spanwise to the wing tip (Fig. 2). Note that the surface following coordinates, s and t, should be scaled such that the line $s = \pi$ occurs at the leading edge of the wing, the line $s = 2\pi$ occurs at the trailing edge of the wing, and the line $t = \pi$ occurs at the wing tip. Also, note that surface following coordinate directions s and t are not necessarily orthogonal to each other.

Evolution model of the top surface of the wing can then be assumed of the form

$$\beta_{ss}\frac{\partial^2}{\partial s^2}\Delta y + \beta_s \frac{\partial}{\partial s}\Delta y + \beta_{tt}\frac{\partial^2}{\partial t^2}\Delta y$$
$$+\beta_t \frac{\partial}{\partial t}\Delta y - \beta_0 \Delta y = \Delta C_p \tag{30}$$

Similarly, the evolution model of the bottom surface of the wing is

$$\beta_{ss}\frac{\partial^2}{\partial s^2}\Delta y - \beta_s \frac{\partial}{\partial s}\Delta y + \beta_{tt}\frac{\partial^2}{\partial t^2}\Delta y$$
$$+\beta_t \frac{\partial}{\partial t}\Delta y - \beta_0 \Delta y = -\Delta C_p \tag{31}$$

The arbitrary globally periodic aerodynamic forcing function, ΔC_p, can be represented using the Fourier series expansion of the form

$$C_p(s,t) =$$
$$\sum_{m=0}^{m_{max}} \sum_{n=0}^{n_{max}} \{[A_{mn}\cos(ns) + B_{mn}\sin(ns)]\cos(mt) + [C_{mn}\cos(ns) + D_{mn}\sin(ns)]\sin(mt)\} \tag{32}$$

The particular solutions to the linear partial differential equations (30) and (31) can be assumed to be of the similar Fourier series form.

$$\Delta y_p^{top}(s,t) =$$
$$\sum_{m=0}^{m_{max}} \sum_{n=0}^{n_{max}} \{[a_{mn}^{top}\cos(ns) + b_{mn}^{top}\sin(ns)]\cos(mt) + [c_{mn}^{top}\cos(ns) + d_{mn}^{top}\sin(ns)]\sin(mt)\} \tag{33}$$

$$\Delta y_p^{bottom}(s,t) =$$
$$\sum_{m=0}^{m_{max}} \sum_{n=0}^{n_{max}} \{[a_{mn}^{bottom}\cos(ns) + b_{mn}^{bottom}\sin(ns)]\cos(mt) + [c_{mn}^{bottom}\cos(ns) + d_{mn}^{bottom}\sin(ns)]\sin(mt)\} \tag{34}$$

Substitution of Eqs. (32) and (33) into Eq. (30) for the top surface of the wing yields

$$\begin{bmatrix} \sigma & n\beta_s & m\beta_t & 0 \\ -n\beta_s & \sigma & 0 & m\beta_t \\ -m\beta_t & 0 & \sigma & n\beta_s \\ 0 & -m\beta_t & -n\beta_s & \sigma \end{bmatrix} \cdot \begin{Bmatrix} a_{mn}^{top} \\ b_{mn}^{top} \\ c_{mn}^{top} \\ d_{mn}^{top} \end{Bmatrix} = \begin{Bmatrix} A_{mn} \\ B_{mn} \\ C_{mn} \\ D_{mn} \end{Bmatrix} \tag{35}$$

where

$$\sigma = -n^2\beta_{ss} - m^2\beta_{tt} - \beta_0 \tag{36}$$

For the special case where the pressure distribution and wing deformation are symmetrical about the wing root t = 0, it follows that

$$C_{mn} = D_{mn} = c_{mn}^{top} = d_{mn}^{top} = 0 \tag{37}$$

$$\begin{bmatrix} \sigma & n\beta_s \\ -n\beta_s & \sigma \\ -m\beta_t & 0 \\ 0 & -m\beta_t \end{bmatrix} \begin{Bmatrix} a_{mn}^{top} \\ b_{mn}^{top} \end{Bmatrix} = \begin{Bmatrix} A_{mn} \\ B_{mn} \\ 0 \\ 0 \end{Bmatrix} \tag{38}$$

Thus,

$$a_{mn}^{top} = \frac{-(n^2\beta_{ss} + m^2\beta_{tt} + \beta_0)A_{mn} - (n\beta_s)B_{mn}}{(n^2\beta_{ss} + m^2\beta_{tt} + \beta_0)^2 + (n\beta_s)^2} \tag{39}$$

$$b_{mn}^{top} = \frac{(n\beta_s)A_{mn} - (n^2\beta_{ss} + m^2\beta_{tt} + \beta_0)B_{mn}}{(n^2\beta_{ss} + m^2\beta_{tt} + \beta_0)^2 + (n\beta_s)^2} \tag{40}$$

$$-m\beta_t = 0 \tag{41}$$

Thus, t-direction damping should not be used.

Similarly, for the bottom surface of the wing,

$$a_{mn}^{bottom} = \frac{(n^2\beta_{ss} + m^2\beta_{tt} + \beta_0)A_{mn} - (n\beta_s)B_{mn}}{(n^2\beta_{ss} + m^2\beta_{tt} + \beta_0)^2 + (n\beta_s)^2} \tag{42}$$

$$b_{mn}^{bottom} = \frac{(n\beta_s)A_{mn} + (n^2\beta_{ss} + m^2\beta_{tt} + \beta_0)B_{mn}}{(n^2\beta_{ss} + m^2\beta_{tt} + \beta_0)^2 + (n\beta_s)^2} \tag{43}$$

As was the case in two dimensions, the differing Fourier coefficients in the particular solutions on the upper and lower surfaces give rise to a gap formation along the leading and trailing edges of the wing.

$$\begin{aligned} Gap_{TE}(t) &= \Delta y_p^{top}(0,t) - \Delta y_p^{bottom}(0,t) \\ &= \sum_{m=0}^{m_{max}} \sum_{n=0}^{n_{max}} [a_{mn}^{top} - a_{mn}^{bottom}]\cos(mt) \\ &= \sum_{m=0}^{m_{max}} \sum_{n=0}^{n_{max}} \frac{-2(n^2\beta_{ss} + m^2\beta_{tt} + \beta_0)A_{mn}\cos(mt)}{(n^2\beta_{ss} + m^2\beta_{tt} + \beta_0)^2 + (n\beta_s)^2} \end{aligned} \tag{44}$$

$$\begin{aligned} Gap_{LE}(t) &= \Delta y_p^{top}(\pi,t) - \Delta y_p^{bottom}(\pi,t) \\ &= \sum_{m=0}^{m_{max}} \sum_{n=0}^{n_{max}} (-1)^n [a_{mn}^{top} - a_{mn}^{bottom}]\cos(mt) \\ &= \sum_{m=0}^{m_{max}} \sum_{n=0}^{n_{max}} \frac{-2(-1)^n(n^2\beta_{ss} + m^2\beta_{tt} + \beta_0)A_{mn}\cos(mt)}{(n^2\beta_{ss} + m^2\beta_{tt} + \beta_0)^2 + (n\beta_s)^2} \end{aligned} \tag{45}$$

There will also be a slope discontinuity that develops at the leading and trailing edges.

$$\begin{aligned} Slope_{TE}(t) &= \frac{\partial}{\partial s}\Delta y_p^{top}(0,t) - \frac{\partial}{\partial s}\Delta y_p^{bottom}(0,t) \\ &= \sum_{m=0}^{m_{max}} \sum_{n=0}^{n_{max}} n[b_{mn}^{top} - b_{mn}^{bottom}]\cos(mt) \\ &\sum_{m=0}^{m_{max}} \sum_{n=0}^{n_{max}} \frac{-2(n^2\beta_{ss} + m^2\beta_{tt} + \beta_0)B_{mn}\cos(mt)}{(n^2\beta_{ss} + m^2\beta_{tt} + \beta_0)^2 + (n\beta_s)^2} \end{aligned} \tag{46}$$

$$\begin{aligned} Slope_{LE}(t) &= \frac{\partial}{\partial s}\Delta y_p^{top}(\pi,t) - \frac{\partial}{\partial s}\Delta y_p^{bottom}(\pi,t) \\ &= \sum_{m=0}^{m_{max}} \sum_{n=0}^{n_{max}} (-1)^n n[b_{mn}^{top} - b_{mn}^{bottom}]\cos(mt) \\ &= \sum_{m=0}^{m_{max}} \sum_{n=0}^{n_{max}} \frac{-2(-1)^n n(n^2\beta_{ss} + m^2\beta_{tt} + \beta_0)B_{mn}\cos(mt)}{(n^2\beta_{ss} + m^2\beta_{tt} + \beta_0)^2 + (n\beta_s)^2} \end{aligned} \tag{47}$$

Series of homogeneous solutions to the shape evolution equations (30) and (31) are used to overcome these gaps. Specifically, on the top surface of the wing, the homogeneous solution should satisfy

$$\begin{aligned} &\beta_{ss}\frac{\partial^2}{\partial s^2}\Delta y_h^{top} + \beta_s\frac{\partial}{\partial s}\Delta y_h^{top} \\ &+ \beta_{tt}\frac{\partial^2}{\partial t^2}\Delta y_h^{top} - \beta_0\Delta y_h^{top} = 0 \end{aligned} \tag{48}$$

The analytic solution of this linear partial differential equation can be found using separation of variables approach.

$$\Delta y_h^{top}(s,t) = S(s)T(t) \tag{49}$$

$$\beta_{ss}\frac{S''}{S} - \beta_s\frac{S'}{S} - \beta_0 = \alpha^2 = -\beta_{tt}\frac{T''}{T} \tag{50}$$

In the T-direction,

$$\beta_{tt}T'' + \alpha^2 T = 0 \tag{51}$$

$$T(t) = (\text{const})\cos(t\sqrt{\frac{\alpha^2}{\beta_{tt}}}) \tag{52}$$

In order to express T as a Fourier series to match modes of gap functions, let

$$\sqrt{\frac{\alpha^2}{\beta_{tt}}} = m, \quad \text{where } m = 0, 1, 2, \ldots \tag{53}$$

Then

$$\alpha^2 = \beta_{tt} m^2 \tag{54}$$

In the S-direction,

$$\beta_{ss}S'' + \beta_s S' - (\beta_0 + \beta_{tt} m^2)S = 0 \tag{55}$$

Let

$$\gamma_m{}^2 = \beta_0 + \beta_{tt} m^2 \tag{56}$$

Then

$$S(s) = (\text{const}_1^{\text{top}})e^{q_m s} + (\text{const}_2^{\text{top}})e^{r_m s} \tag{57}$$

where

$$q_m = \frac{-\beta_s + \sqrt{\beta_s{}^2 + 4\gamma_m{}^2\beta_{ss}}}{2\beta_{ss}} \tag{58}$$

$$r_m = \frac{-\beta_s - \sqrt{\beta_s{}^2 + 4\gamma_m{}^2\beta_{ss}}}{2\beta_{ss}} \tag{59}$$

Then, on the upper surface of the wing, the y-coordinate correction due to the homogeneous solution is

$$\Delta y_h^{\text{top}} = \sum_{m=0}^{m_{max}} [(\bar{E}_m^{\text{top}} e^{q_m s} + \bar{F}_m^{\text{top}} e^{r_m s})\cos(mt)] \tag{60}$$

For later convenience, multiples are extracted from the E and F constants on the top surface, giving

$$\Delta y_h^{\text{top}} = \sum_{m=0}^{m_{max}} \{[E_m^{\text{top}} e^{-q_m(2\pi - s)} + F_m^{\text{top}} e^{-r_m(2\pi - s)}]\cos(mt)\} \tag{61}$$

Similarly, on the bottom surface of the wing,

$$\Delta y_h^{\text{bottom}} = \sum_{m=0}^{m_{max}} [(E_m^{\text{bottom}} e^{-q_m s} + F_m^{\text{bottom}} e^{-r_m s})\cos(mt)] \tag{62}$$

To eliminate the trailing edge gap in each mode,

$$\Delta y_h^{\text{top}}(2\pi, t) - \Delta y_h^{\text{bottom}}(0, t) = -\text{Gap}_{TE}(t) \tag{63}$$

From Eqs. (61) and (62) this condition is satisfied when

$$E_m^{\text{top}} + F_m^{\text{top}} - E_m^{\text{bottom}} - F_m^{\text{bottom}} = \sum_{n=0}^{n_{max}} \frac{2(n^2\beta_{ss} + m^2\beta_{tt} + \beta_0)A_{mn}}{(n^2\beta_{ss} + m^2\beta_{tt} + \beta_0)^2 + (n\beta_s)^2} \tag{64}$$

To eliminate the slope discontinuity at the trailing edge in each mode,

$$\frac{\partial}{\partial s}\Delta y_h^{\text{top}}(2\pi, t) - \frac{\partial}{\partial s}\Delta y_h^{\text{bottom}}(0, t) = -\text{Slope}_{TE}(t) \tag{65}$$

From Eqs. (61) and (62) this condition is satisfied when

$$E_m^{\text{top}} q_m + G_m^{\text{top}} r_m + E_m^{\text{bottom}} q_m + F_m^{\text{bottom}} r_m = \sum_{n=0}^{n_{max}} \frac{2n(n^2\beta_{ss} + m^2\beta_{tt} + \beta_0)B_{mn}}{(n^2\beta_{ss} + m^2\beta_{tt} + \beta_0)^2 + (n\beta_s)^2} \tag{66}$$

To eliminate the leading edge gap in each mode,

$$\Delta y_h^{\text{top}}(\pi, t) - \Delta y_h^{\text{bottom}}(\pi, t) = -\text{Gap}_{LE}(t) \tag{67}$$

From Eqs. (60) and (62) this condition is satisfied when

$$E_m^{\text{top}} e^{-\pi q_m} + F_m^{\text{top}} e^{-\pi r_m} - E_m^{\text{bottom}} e^{-\pi q_m} - F_m^{\text{bottom}} e^{-\pi r_m} = \sum_{n=0}^{n_{max}} \frac{2(-1)^n(n^2\beta_{ss} + m^2\beta_{tt} + \beta_0)A_{mn}}{(n^2\beta_{ss} + m^2\beta_{tt} + \beta_0)^2 + (n\beta_s)^2} \tag{68}$$

To eliminate the slope discontinuity at the leading edge in each mode,

$$\frac{\partial}{\partial s}\Delta y_h^{\text{top}}(\pi, t) - \frac{\partial}{\partial s}\Delta y_h^{\text{bottom}}(\pi, t) = -\text{Slope}_{LE}(t) \tag{69}$$

From Eqs. (60) and (62) this condition is satisfied when

$$E_m^{top} q_m e^{-\pi q_m} + F_m^{top} r_m e^{-\pi r_m} + E_m^{bottom} q_m e^{-\pi q_m} + F_m^{bottom} r_m e^{-\pi r_m} = \sum_{n=0}^{n_{max}} \frac{2n(-1)^n (n^2\beta_{ss} + m^2\beta_{tt} + \beta_0) B_{mn}}{(n^2\beta_{ss} + m^2\beta_{tt} + \beta_0)^2 + (n\beta_s)^2} \quad (70)$$

Combining the boundary conditions yields a 4 x 4 matrix equation for E and F coefficients in each mode, m.

$$\begin{bmatrix} 1 & 1 & -1 & -1 \\ q_m & r_m & q_m & r_m \\ e^{-\pi q_m} & e^{-\pi r_m} & -e^{-\pi q_m} & -e^{-\pi r_m} \\ q_m e^{-\pi q_m} & r_m e^{-\pi r_m} & q_m e^{-\pi q_m} & r_m e^{-\pi r_m} \end{bmatrix} \begin{Bmatrix} E_m^{top} \\ F_m^{top} \\ E_m^{bottom} \\ F_m^{bottom} \end{Bmatrix}$$

$$= \begin{Bmatrix} \sum_{n=0}^{n_{max}} \frac{2(n^2\beta_{ss} + m^2\beta_{tt} + \beta_0) A_{mn}}{(n^2\beta_{ss} + m^2\beta_{tt} + \beta_0)^2 + (n\beta_s)^2} \\ \sum_{n=0}^{n_{max}} \frac{2n(n^2\beta_{ss} + m^2\beta_{tt} + \beta_0) B_{mn}}{(n^2\beta_{ss} + m^2\beta_{tt} + \beta_0)^2 + (n\beta_s)^2} \\ \sum_{n=0}^{n_{max}} \frac{2(-1)^n (n^2\beta_{ss} + m^2\beta_{tt} + \beta_0) A_{mn}}{(n^2\beta_{ss} + m^2\beta_{tt} + \beta_0)^2 + (n\beta_s)^2} \\ \sum_{n=0}^{n_{max}} \frac{2n(-1)^n (n^2\beta_{ss} + m^2\beta_{tt} + \beta_0) B_{mn}}{(n^2\beta_{ss} + m^2\beta_{tt} + \beta_0)^2 + (n\beta_s)^2} \end{Bmatrix} \quad (71)$$

This matrix equation becomes stiffer with increasing mode number, m. Thus, a numerical inversion is not suggested. The constants can however be calculated analytically. Let

$$\begin{Bmatrix} rhs_1 \\ rhs_2 \\ rhs_3 \\ rhs_4 \end{Bmatrix} = \begin{Bmatrix} \sum_{n=0}^{n_{max}} \frac{2(n^2\beta_{ss} + m^2\beta_{tt} + \beta_0) A_{mn}}{(n^2\beta_{ss} + m^2\beta_{tt} + \beta_0)^2 + (n\beta_s)^2} \\ \sum_{n=0}^{n_{max}} \frac{2n(n^2\beta_{ss} + m^2\beta_{tt} + \beta_0) B_{mn}}{(n^2\beta_{ss} + m^2\beta_{tt} + \beta_0)^2 + (n\beta_s)^2} \\ \sum_{n=0}^{n_{max}} \frac{2(-1)^n (n^2\beta_{ss} + m^2\beta_{tt} + \beta_0) A_{mn}}{(n^2\beta_{ss} + m^2\beta_{tt} + \beta_0)^2 + (n\beta_s)^2} \\ \sum_{n=0}^{n_{max}} \frac{2n(-1)^n (n^2\beta_{ss} + m^2\beta_{tt} + \beta_0) B_{mn}}{(n^2\beta_{ss} + m^2\beta_{tt} + \beta_0)^2 + (n\beta_s)^2} \end{Bmatrix} \quad (72)$$

Then

$$E_m^{top} = \frac{1}{2} \begin{bmatrix} rhs_1 + \frac{rhs_1 e^{-\pi q_m} - rhs_3}{e^{-\pi r_m} - e^{-\pi q_m}} \\ + \frac{rhs_2}{q_m} + \frac{rhs_2 e^{-\pi q_m} - rhs_4}{r_1 (e^{-\pi r_m} - e^{-\pi q_m})} \end{bmatrix} \quad (73)$$

$$F_m^{top} = \frac{1}{2} \left[\frac{rhs_4 - rhs_2 e^{-\pi q_m}}{r_m (e^{-\pi r_m} - e^{-\pi q_m})} + \frac{rhs_3 - rhs_1 e^{-\pi q_m}}{e^{-\pi r_m} - e^{-\pi q_m}} \right] \quad (74)$$

$$E_m^{bottom} = \frac{1}{2} \begin{bmatrix} -rhs_1 - \frac{rhs_1 e^{-\pi q_m} - rhs_3}{e^{-\pi r_m} - e^{-\pi q_m}} \\ + \frac{rhs_2}{q_m} + \frac{rhs_2 e^{-\pi q_m} - rhs_4}{q_m (e^{-\pi r_m} - e^{-\pi q_m})} \end{bmatrix} \quad (75)$$

$$F_m^{bottom} = \frac{1}{2} \left[\frac{rhs_4 - rhs_2 e^{-\pi q_m}}{r_m (e^{-\pi r_m} - e^{-\pi q_m})} - \frac{rhs_3 - rhs_1 e^{-\pi q_m}}{e^{-\pi r_m} - e^{-\pi q_m}} \right] \quad (76)$$

Finally,

$$\Delta y^{top}(s,t) = \sum_{m=0}^{m_{max}} \begin{pmatrix} [E_m^{top} e^{-q_m(2\pi - s)} + F_m^{top} e^{-r_m(2\pi - s)}] \cos(mt) + \\ \sum_{n=0}^{n_{max}} \{ [a_{mn}^{top} \cos(ns) + b_{mn}^{top} \sin(ns)] \cos(mt) + \\ [c_{mn}^{top} \cos(ns) + d_{mn}^{top} \sin(ns)] \sin(mt) \} \end{pmatrix} \quad (77)$$

$$\Delta y^{bottom}(s,t) = \sum_{m=0}^{m_{max}} \begin{pmatrix} [E_m^{bottom} e^{-q_m s} + F_m^{bottom} e^{-r_m s}] \cos(mt) + \\ \sum_{n=0}^{n_{max}} \{ [a_{mn}^{bottom} \cos(ns) + b_{mn}^{bottom} \sin(ns)] \cos(mt) \\ + [c_{mn}^{bottom} \cos(ns) + d_{mn}^{bottom} \sin(ns)] \sin(mt) \} \end{pmatrix} \quad (78)$$

IV. Numerical Results

A. Two-dimensional Airfoil Inverse Design Results

The airfoil design case utilized a target coefficient of pressure distribution corresponding to a NACA 1311 cambered airfoil at free stream Mach number M = 0.5. The initial geometry was a NACA 0012 non-lifting airfoil. Shape evolution parameters β_{ss}, β_s, and β_0 were set to 1.2, 0.0, and 0.4 respectively. The evolution of the airfoil surface coefficient of pressure distribution and its geometry are shown[16-18] in Figs. 3 and 4.

Three flow-field analysis codes (a potential flow code with Laitone's algebraic compressibility correction, an Euler compressible flow code, and a compressible viscous flow Navier-Stokes code with a Baldwin-Lomax turbulence model) were used to demonstrate that the Fourier series technique converges consistently faster than the original MGM technique especially with the Euler and the Navier-Stokes flow-field analysis codes (Fig. 5).

B. Three-dimensional Wing Inverse Design Results

After verifying that the three-dimensional version of the Fourier series method maintains symmetry when designing a wing with a symmetric surface pressure distribution at every station[17,18], an inverse design test case was carried out using a three-dimensional surface panel flow-field analysis code with an algebraic compressibility correction.

The objective was to test the Fourier technique's ability to simultaneously modify a wing's spanwise distribution of thickness, camber, twist, and dihedral. Only the trailing edge point of the wing root section was fixed. The wing had a taper ratio of 0.5 and a leading edge backward sweep angle of 7.125 degrees. The semi-span was equal to two root chord lengths. The wing tip airfoil had a non-zero thickness and free-stream Mach number was M = 0.2. The target pressure distribution was obtained from analysis of a wing having a NACA 1311 root airfoil and a NACA 2412 tip airfoil. The target wing had a linearly varying twist with 0.0 angle of attack at the root and +3.0 degrees angle of attack at the wing tip. The initial geometry had a constant NACA 0009 airfoil shape with a linearly varying twist angle from 0.0 degrees at the root to –1.0 degree angle of attack at the tip. The wing grid had 64 panels in the s-direction and 19 panels in the span-wise direction that were clustered toward the wing tip. The shape evolution parameters β_{tt}, β_{ss}, β_{s}, and β_0 were set to 7.0, 0.9, 0.0, and 1.2. The maximum number of Fourier terms considered in the s- and t-directions, were set to n_{max} =120 and m_{max} = 120. After ten design iterations, the target pressure differs mostly near the wing tip and at the trailing edge (Fig. 6). The evolution of the wing shape is shown in Fig.7.

The next test case was examined in conjunction with both a three-dimensional turbulent Navier-Stokes flow-field analysis code and an Euler flow-field analysis code. In these cases, a wing tip that quickly shrinks the airfoil thickness down to zero was added to each wing. The wing had a taper ratio of 0.5. The leading edge sweep angle was 14.03 degrees and the trailing edge had zero sweep, while the semi-span was two times the root chord length. The free stream Mach number was M = 0.6. The computational grid was regenerated after each application of the Fourier series design method by stacking two-dimensional C-grids generated for each span station. Twenty span stations, 32 C-layers, 64 grid cells on each airfoil, and 16 cells along the wake defined the computational grid. A turbulent Navier-Stokes flow-field analysis code with Reynolds number of one million was used to obtain the target pressure distribution corresponding to a severely twisted wing with a root airfoil NACA 0009 at +4.0 degrees angle of attack and a tip airfoil NACA 1311 at –4.0 degrees angle of attack. The initial geometry for the design process had root airfoil NACA 2412 at –4.0 degrees angle of attack and a tip airfoil NACA0009 at +4.0 degrees angle of attack. The shape evolution parameters β_{tt}, β_{ss}, β_{s}, and β_0 were set to 7.0, 0.9, 0.0, and 1.2, respectively. The target pressure distribution (Fig. 8) is not fully achieved near the root and tip after 20 design iterations. Figure 9 depicts the change in wing geometry including dihedral angle during the design process. The same test case was then repeated with an Euler flow-field analysis code where the viscosity effects were not included in the target pressure distribution. When using the same shape evolution parameters β_{tt}, β_{ss}, β_{s}, and β_0, the inverse design convergence rates when using the Euler code and the Navier-Stokes code were basically the same.

Next, an Euler equation design case was performed in transonic flight conditions, seeking to design a fully subsonic wing from an initial wing with a shock wave at the flight Mach number M = 0.8. The wing planform had a taper ratio of 0.5, leading edge sweep angle of 14.03 degrees, zero trailing edge sweep, and semi-span of two times the root chord length. The initial guess had a NACA 0012 airfoil shape at +5.0 degrees angle of attack. The target pressure distribution corresponded to a non-lifting wing with a NACA 0009 airfoil. The computational grid was defined by 20 span stations, 32 C-layers, and 100 grid cells per airfoil. The shape evolution parameters β_{tt}, β_{ss}, β_{s}, and β_0 were set to 7.0, 1.2, 1.0, and 1.6, respectively. After twenty iterations, the wing still had some lift (Fig. 10) despite its non-lifting target pressure distribution. The airfoil shape obtained after the first iteration of the Fourier series technique developed a dent at the location of the shock wave on the upper surface of the wing (Fig.11). However, after 20 iterations in this case, the concavity was removed, leaving a smooth wing shape (Fig. 11) and no shock wave (Fig. 12).

Finally, an Euler design of a shocked wing was attempted by performing a reverse of the previous case, that is, by designing a wing at +5.0 degrees angle of attack with a NACA 0012 airfoil from an initial wing at zero incidence with a NACA 0009 airfoil. The shape evolution parameters were β_{tt} = 7.0, β_{ss} = 0.7, β_{s} = 3.0, β_0 = 1.4. The shock location history (Fig. 13) shows that the shock wave location stabilizes after a few iterations of the Fourier series technique in this case. The evolution of the surface coefficient of pressure distributions at several span stations (Fig. 14) and evolution of the wing geometry still underwent a significant waving motion when using damping (Fig. 15).

V. Conclusions

A mathematical formulation for the elastic membrane concept in aerodynamic shape inverse design using an analytical Fourier series solution has been developed. A benefit of the Fourier technique is that it requires no modification to the existing flow-field analysis software. In two dimensions, numerical results have shown that the

Fourier technique converges considerably faster than the MGM method from which it was derived. The original MGM design method uses finite differencing to evaluate derivatives in the surface evolution equation while Fourier method uses analytic expressions. The Fourier series method does not appear to suffer from slower convergence due to increases in the non-linearity of the flow-field analysis code. The Fourier technique requires the user to specify several constants that can affect the convergence if selected poorly. In three dimensions, numerical results have shown that subsonic wings can be reliably designed using a panel code, an Euler solver, or a turbulent Navier-Stokes solver. Transonic cases in three dimensions have demonstrated the necessity of s-directional damping in the shape evolution equation, as without damping, the surface of the aerodynamic body is prone to oscillate excessively in the vicinity of shock waves.

Acknowledgments

The authors are grateful for a NASA Langley Graduate Student Fellowship facilitated by Dr. John Malone, National Science Foundation Grant DMI-9522854 monitored by Dr. George Hazelrigg, NASA Lewis Research Center Grant NAG3-1995 facilitated by Dr. John Lytle, and supervised by Dr. Kestutis Civinskas, Lawrence Livermore National Laboratory subcontract B344847 monitored by Dr. J. Ray Smith, and Dr. K. Kubrynski for the use of his three-dimensional surface panel flow-field analysis code.

References

[1]Dulikravich, G. S., "Shape Inverse Design and Optimization for Three-Dimensional Aerodynamics," AIAA invited paper 95-0695, AIAA Aerospace Sciences Meeting, Reno, NV, January 1995.

[2]Dulikravich, G. S., "Aerodynamic Shape Design and Optimization: Status and Trends, *AIAA Journal of Aircraft*," Vol. 29, No. 5, 1992, pp. 1020-1026.

[3]Dulikravich, G. S., "Design and Optimization Tools Development," chapters no. 10-15 in *New Design Concepts for High Speed Air Transport*, (editor: H. Sobieczky), Springer, New York, 1997, pp. 159-236.

[4]Fujii, K., and Dulikravich, G. S. (editors): *Recent Development of Aerodynamic Design Methodologies - Inverse Design and Optimization*, Vieweg Series on *Notes on Numerical Fluid Mechanics*, Springer, 1999.

[5]Dulikravich, G. S. (editor): *Proceedings of the Third International Conference on Inverse Design Concepts and Optimization in Engineering Sciences (ICIDES-III)*, Washington, D.C., October 23-25, 1991; also NASA CR-188125, January 1992.

[6]Dulikravich, G. S. (editor): *Proceedings of the Second International Conference on Inverse Design Concepts and Optimization in Engineering Sciences (ICIDES-II)*, The Pennsylvania State University, University Park, PA, October 26-28, 1987.

[7]Dulikravich, G. S., (editor): *Proceedings of the First International Conference on Inverse Design Concepts in Engineering Sciences (ICIDES-I)*, University of Texas at Austin, College of Engineering, October 17-18, 1984.

[8]Tanaka, M., and Dulikravich, G. S. (editors): *Inverse Problems in Engineering Mechanics (ISIP'98)*, Elsevier Science Ltd., U.K., 1998.

[9]Garabedian, P., and McFadden, G., "Design of Supercritical Swept Wings," *AIAA Journal*, Vol. 20, No. 3, March 1982, pp. 289-291.

[10]Garabedian, P., and McFadden, G., "Computational Fluid dynamics of Airfoils and Wings," in *Transonic, Shock, and Multi-dimensional Flows: Advances in Scientific Computing*, Academic Press, 1982, pp. 1-16.

[11]Malone, J. B., Vadyak, J., and Sankar, L. N., "A Technique for the Inverse Aerodynamic Design of Nacelles and Wing Configurations," *AIAA Journal of Aircraft*, Vol. 24, No. 1, January 1987, pp. 8-9.

[12]Hazarika, N., "An Efficient Inverse Method for the Design of Blended Wing-Body Configurations," Ph.D. Thesis, Aerospace Eng. Dept., Georgia Institute of Technology, June 1988.

[13]Malone, J. B., Narramore, J. C., and Sankar, L. N., "An Efficient Airfoil Design Method Using the Navier-Stokes Equations," in *Proceedings of AGARD Specialists' Meeting on Computational Methods for Aerodynamic Design (Inverse) and Optimization*, AGARD-CP-463, (editor: J. Slooff), Loen, Norway, May 1989.

[14]Malone, J. B., Narramore, J. C., and Sankar, L. N., "An Airfoil Design Method for Viscous Flows," *Proceedings of the 15th Southeastern Conference on Theoretical and Applied Mechanics*, (editors: S. V. Hanagud, M. P. Kamat, C. E. Ueng), Georgia Institute of Technology, Atlanta, GA Vol. XV, 1990, pp. 463-470.

[15]Yu, N. J., and Campbell, R. L., "Transonic Airfoil and Wing Design Using Navier-Stokes Codes," AIAA paper 92-2651, 1992.

[16]Dulikravich, G. S., and Baker, D. P., "Fourier Series Analytical Solution for Inverse Design of Aerodynamic Shapes," in *Inverse Problems in Engineering Mechanics (ISIP'98)*, (editors: M. Tanaka and G.S. Dulikravich), Nagano, Japan, March 24-27, 1998, Elsevier Science Ltd, U.K., 1998, pp. 427-436.

[17]Dulikravich, G. S., and Baker, D. P., "Using Existing Flow-Field Analysis Codes for Inverse Design of Three-dimensional Aerodynamic Shapes," a chapter in *Recent Development of Aerodynamic Design Methodologies - Inverse Design and Optimization*, (editors: Fujii, K. and Dulikravich, G. S.), Vieweg Series on *Notes on Numerical Fluid Mechanics*, Springer, 1999.

[18]Baker, D. P., "A Fourier Series Approach to the Elastic Membrane Inverse Shape Design Problem in Aerodynamics", M.Sc. Thesis, Dept. of Aerospace Eng., The Pennsylvania State University, May 1999.

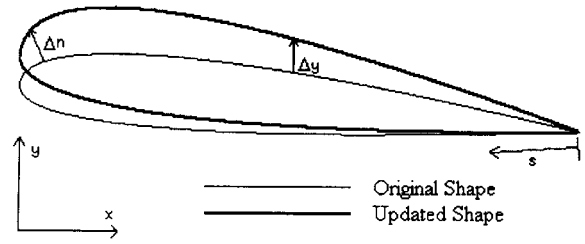

Fig. 1 Airfoil contour following coordinate, s, contour corrections Δn and Δy, and the Cartesian system x,y.

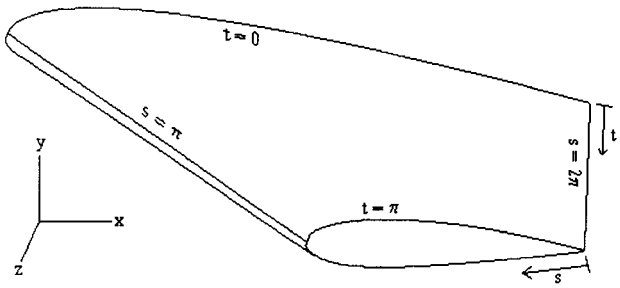

Fig. 2 Wing surface following coordinates s,t and the Cartesian coordinate system x,y,x.

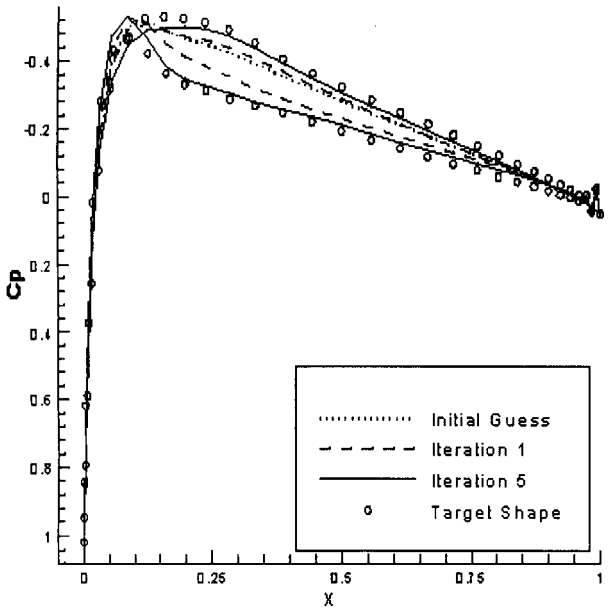

Fig. 3 Coefficient of surface pressure evolution for an isolated cambered airfoil using Navier-Stokes flow-field analysis code.

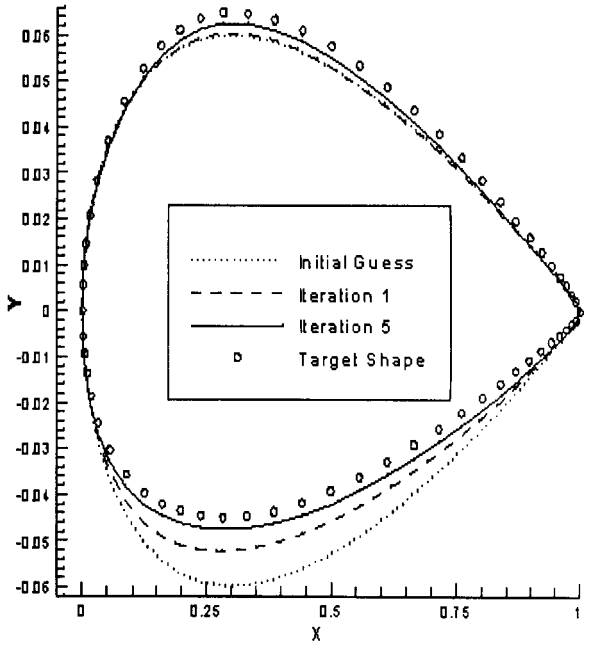

Fig. 3 Geometry evolution of an isolated cambered airfoil using Navier-Stokes flow-field analysis code.

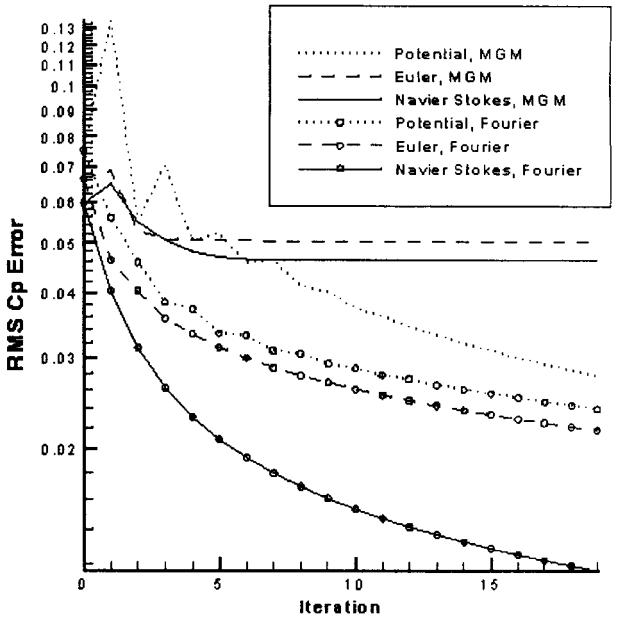

Fig. 5 Comparison of convergence histories for the classical MGM and the Fourier series inverse shape design methods. Initial guess is a NACA0012 airfoil. Target is a NACA1311 airfoil at M = 0.5, Re = 1000000, $\beta_{ss} = 1.2$, $\beta_s = 0.0$, $\beta_0 = 0.4$.

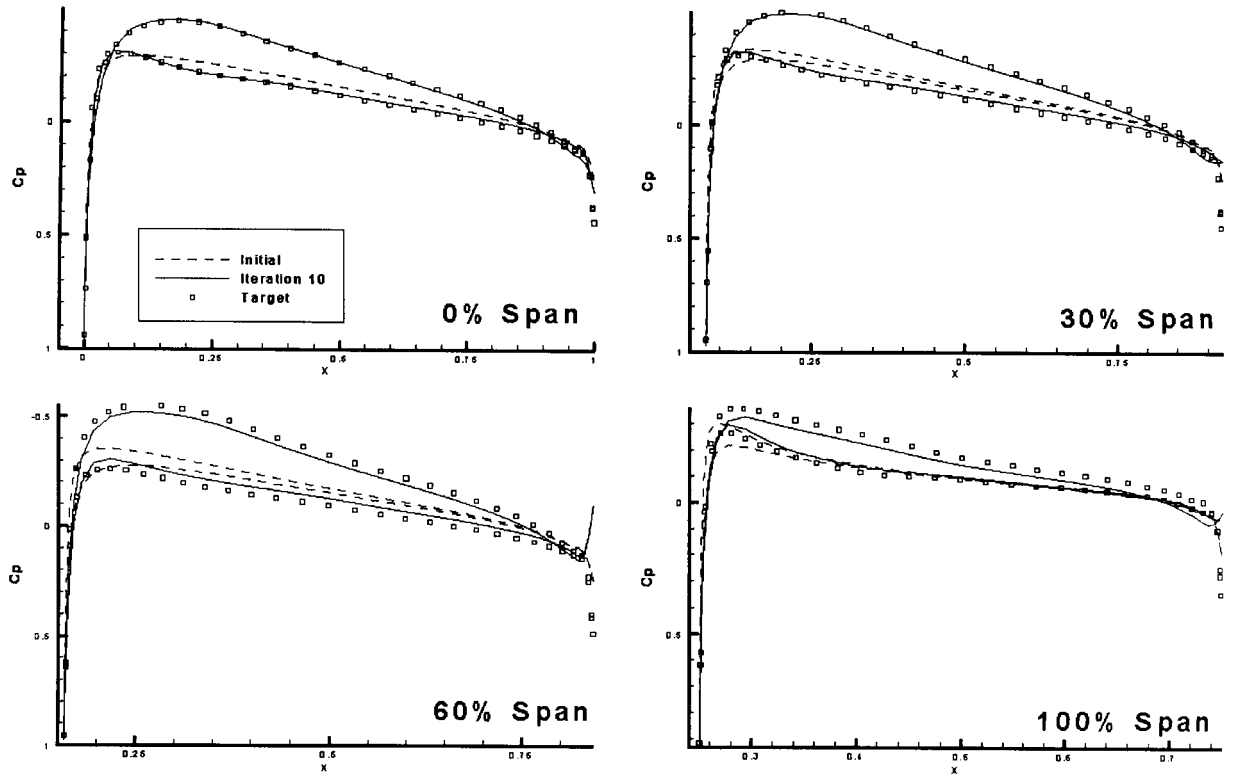

Fig. 6 Section-wise surface coefficient of pressure evolution for a subsonic wing design using a surface panel flow-field analysis code.

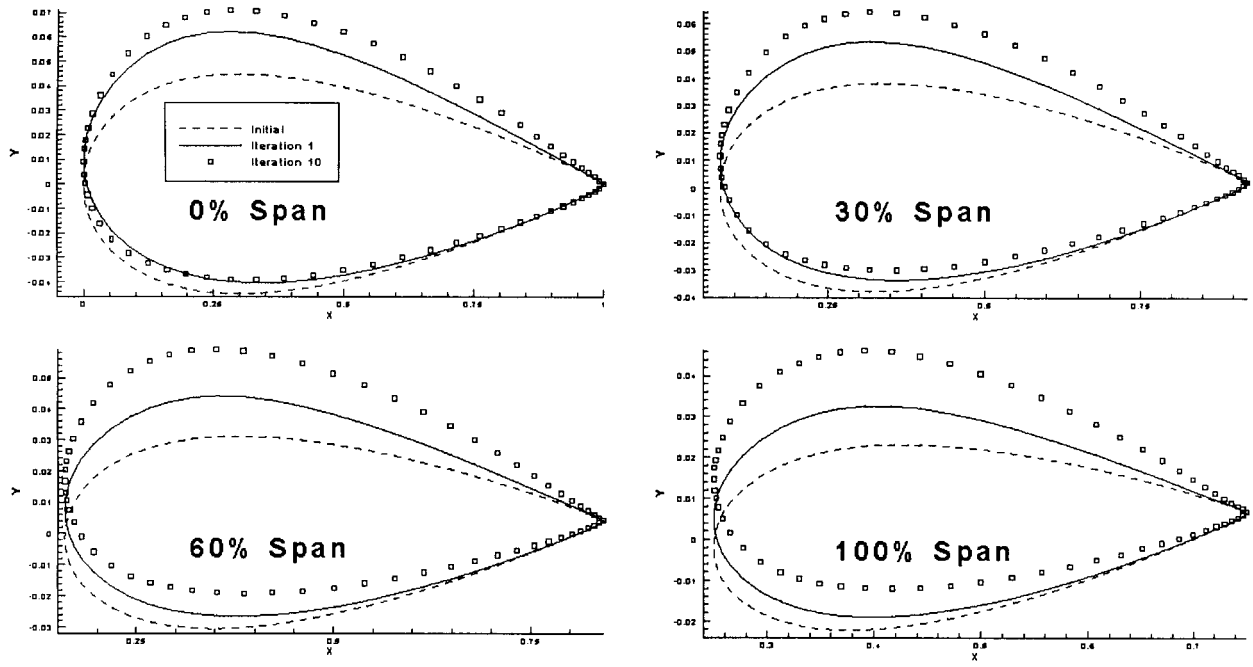

Fig. 7 Section-wise geometry evolution for a subsonic wing design using a surface panel flow-field analysis code.

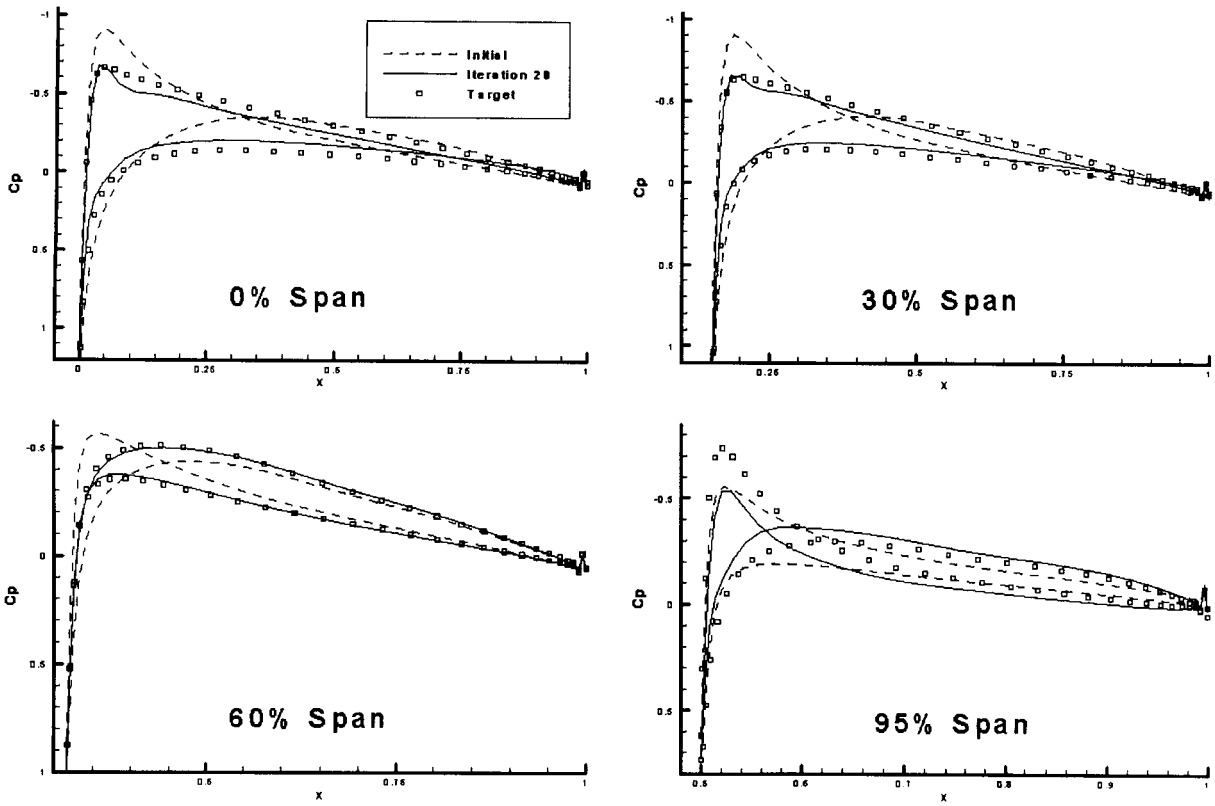

Fig. 8 Section-wise surface coefficient of pressure evolution for a severely twisted subsonic wing design using a Navier-Stokes flow-field analysis code.

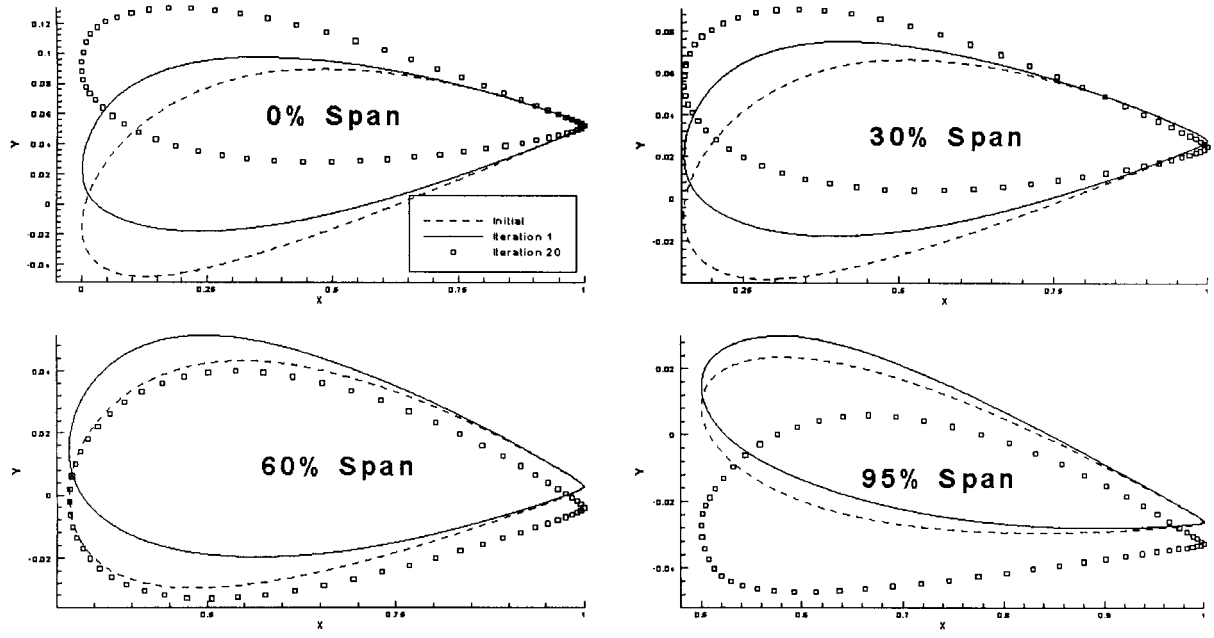

Fig. 9 Section-wise geometry evolution for a severely twisted subsonic wing design using a Navier-Stokes flow-field analysis code.

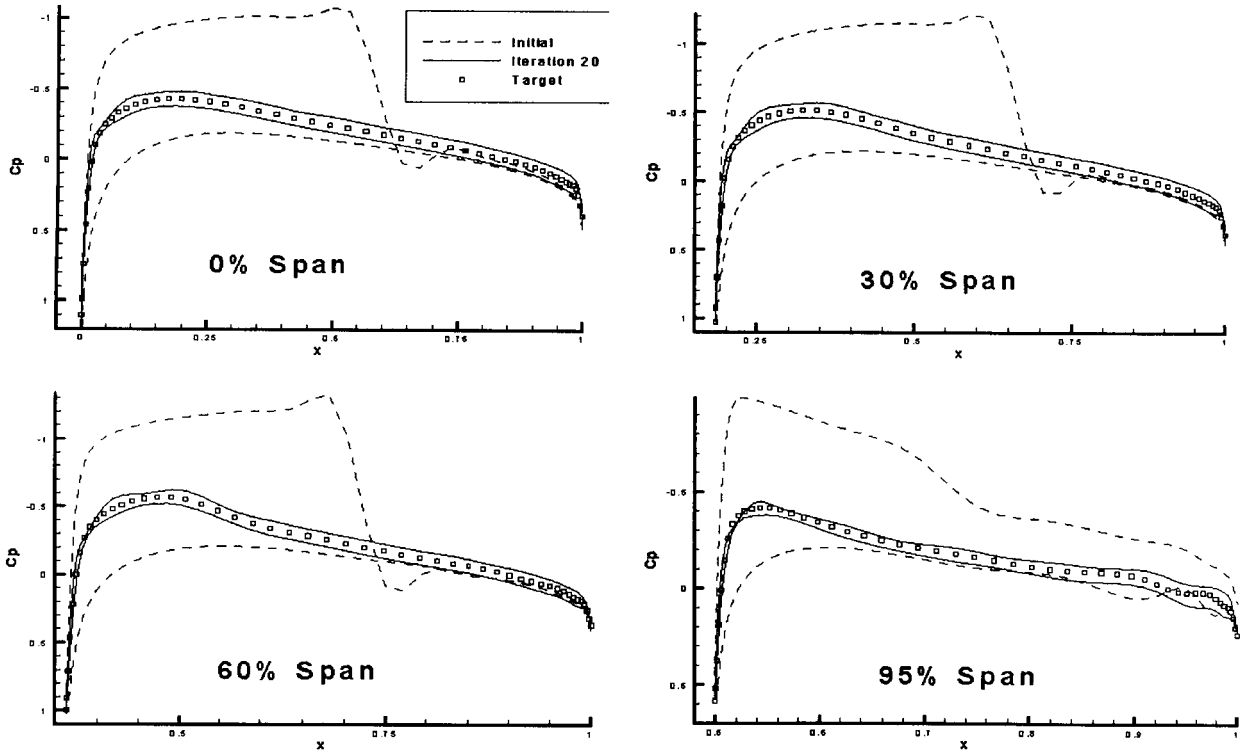

Fig. 10 Section-wise surface coefficient of pressure evolution for an initially shocked transonic wing using an Euler flow-field analysis code.

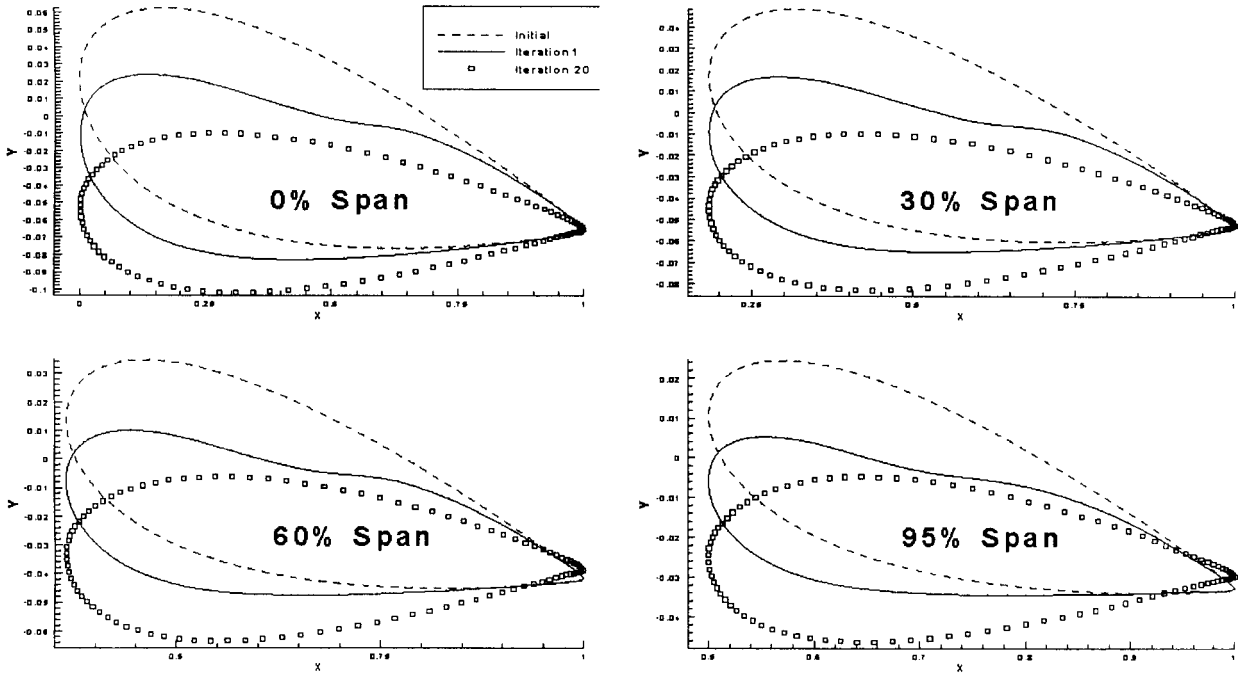

Fig. 11 Section-wise geometry evolution for an initially shocked transonic wing using an Euler flow-field analysis code.

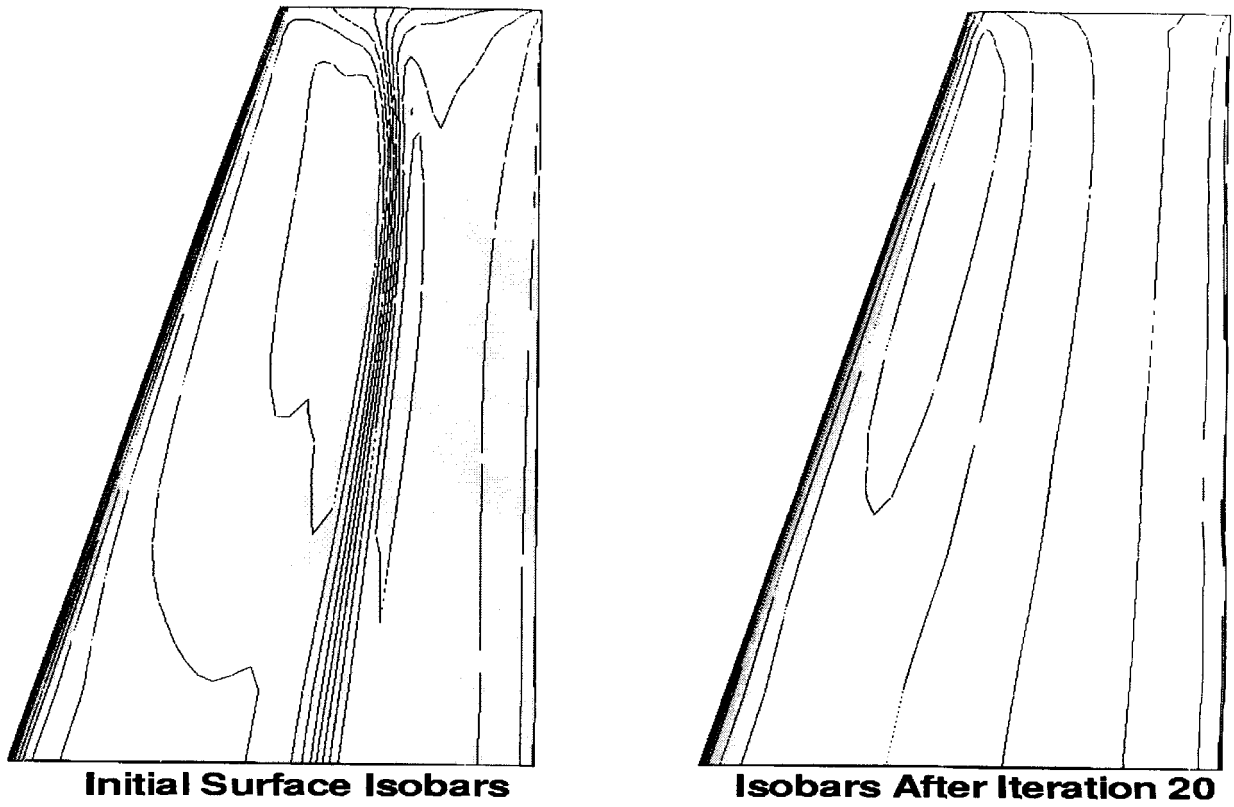

Fig. 12 Initial and inversely designed wing top surface isobars for an initially shocked transonic wing using an Euler flow-field analysis code in conjunction with the Fourier series inverse design technique.

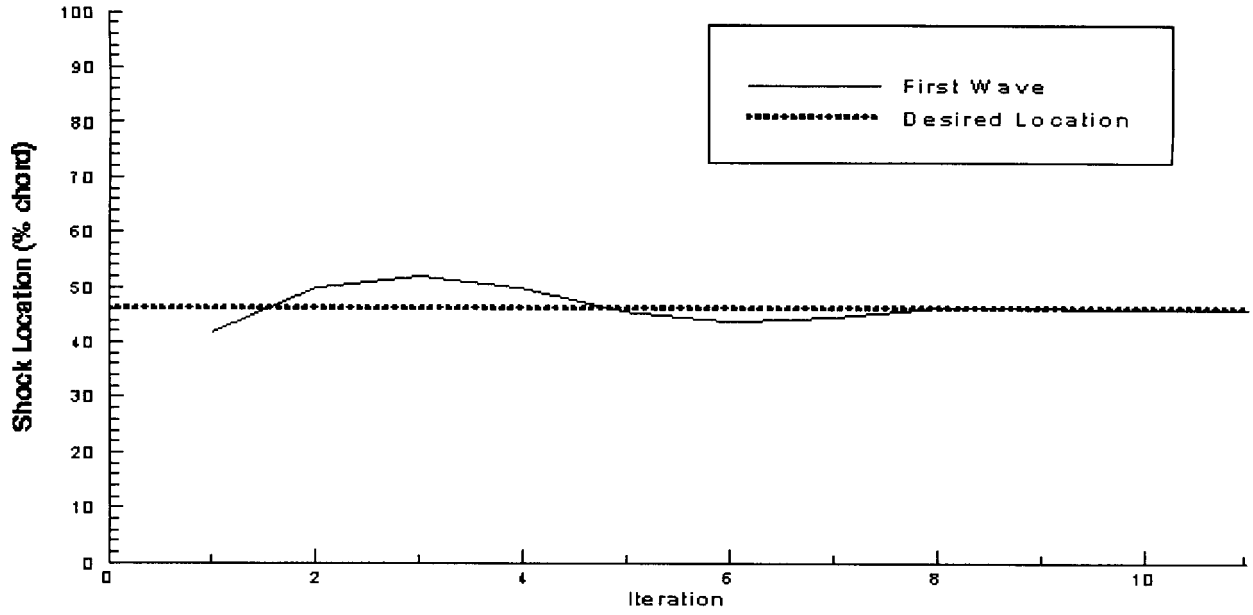

Fig. 13 Shock wave migration at 75% wing span location for an inverse design of a transonic wing with a shock.

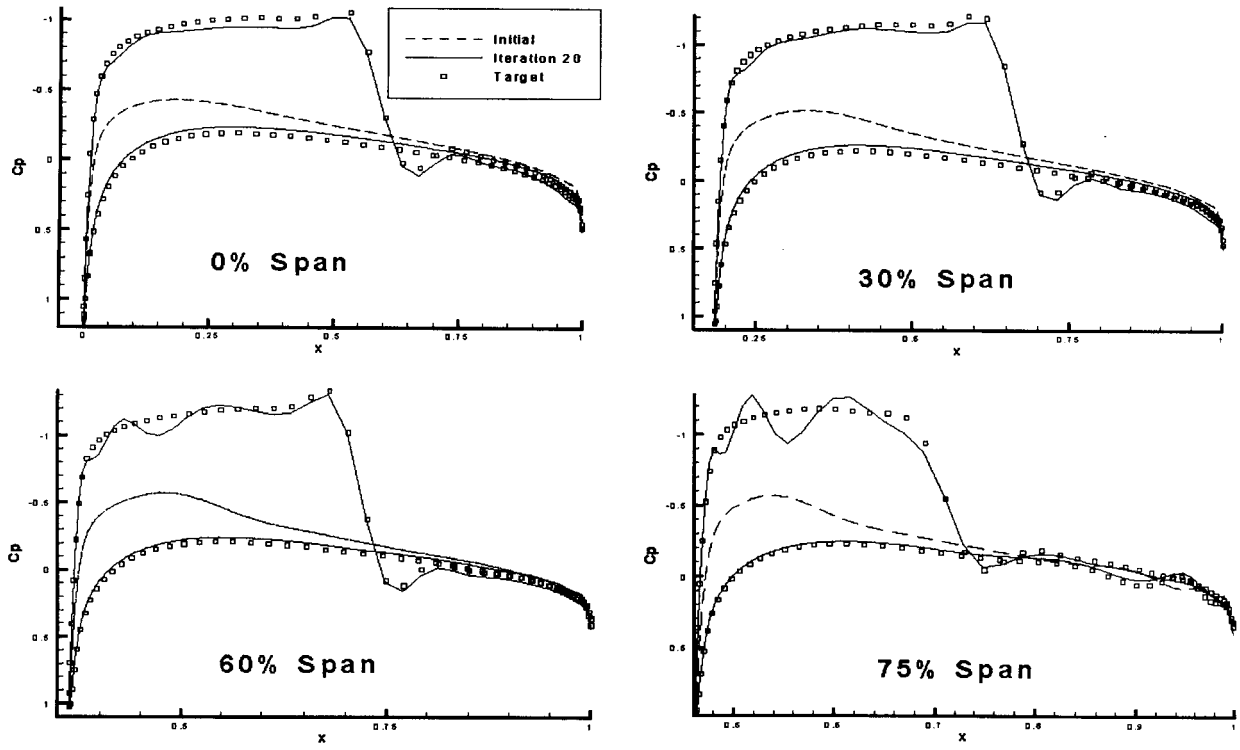

Fig. 14 Span-wise evolution of surface coefficient of pressure for a wing design having a specified three-dimensional shock wave. An Euler flow-field analysis code was used in conjunction with the Fourier series inverse shape design technique.

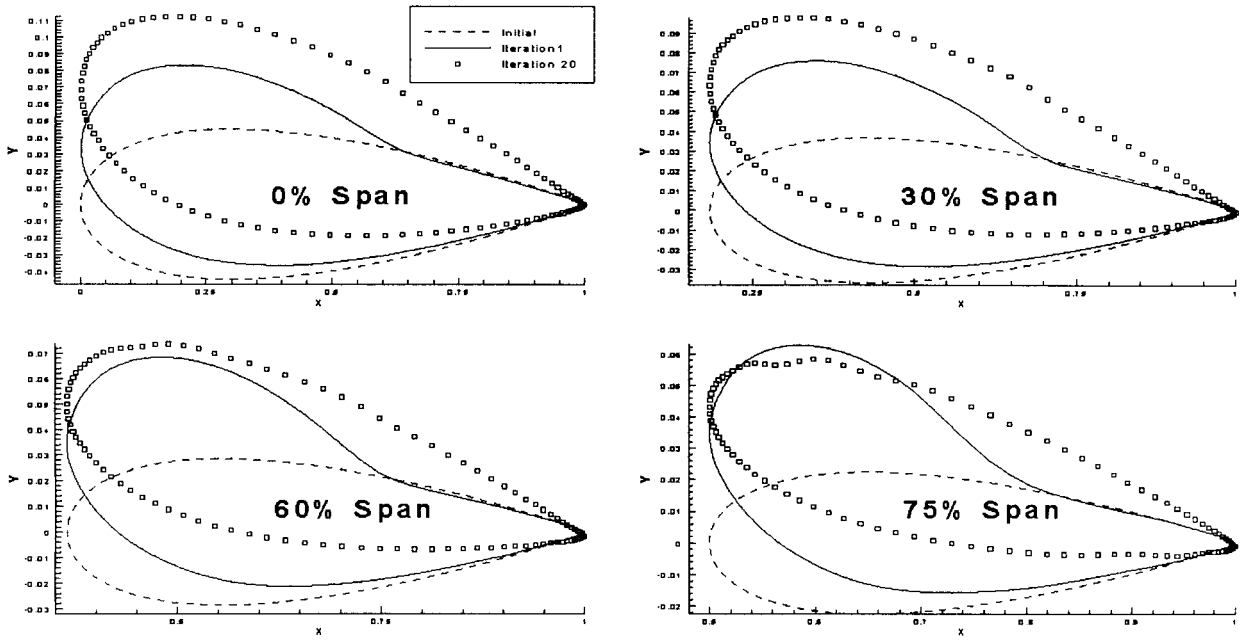

Fig. 15 Span-wise geometry evolution for a wing design having a specified three-dimensional shock wave. An Euler flow-field analysis code was used in conjunction with the Fourier series inverse shape design technique.